Local variability of vegetation structure increases forest resilience to wildfire

Michael J. Koontz[1,2], Malcolm P. North[2,3], Chhaya M. Werner[2,4], Stephen E. Fick[5,6], Andrew M. Latimer[2]

[1]Graduate Group in Ecology, University of California; Davis, CA
[2]Department of Plant Sciences, University of California; Davis, CA
[3]Pacific Southwest Research Station, U.S.D.A. Forest Service; Davis, CA
[4]Center for Population Biology, University of California; Davis, CA
[5]U.S. Geological Survey, Southwest Biological Science Center
[6]Department of Ecology and Evolutionary Biology, University of Colorado; Boulder, CO

Abstract: The long-term persistence of forest ecosystems hinges on their resilience to ongoing disturbance. Quantification of resilience in these valuable ecosystems remains difficult due to their vast extent and the longevity of forest species. Resilience to wildfire may arise from feedback between fire behavior and vegetation structure, which dictates fuel loading and continuity. Regular fire generates structural variability which may then enable forests to withstand future fires and retain their fundamental properties and functions– a hallmark of a resilient system. A century of fire suppression in the western United States has homogenized the structure of many forests, potentially upsetting these feedbacks and compromising forest resilience. We investigate the generality and scale of the effect of structural variability on wildfire behavior in yellow pine/mixed-conifer forest of California's Sierra Nevada using cloud computing and texture analysis of a 33-year time series of satellite imagery. We measure wildfire response to forest structure for an unprecedented number and size range of wildfires, ensuring representation of both typical and extreme fire behavior, and find that greater structural variability is strongly associated with a lower probability of fire-induced overstory tree mortality. This resistance to wildfire was most apparent at the smallest spatial extent of forest structure tested (90m x 90m). Local-scale structural variability thus links past and future fire behavior, and makes forests more resilient to wildfire disturbance. Management strategies that increase vegetation structural variability, such as allowing fires to burn under moderate fuel and weather conditions, may therefore increase the probability of long-term forest persistence.

Significance

A "resilient" forest endures disturbance and is likely to persist. Resilience to wildfire may derive from variability in vegetation structure, which interrupts fuel continuity and prevents fire from killing overstory trees. Testing the generality and scale of this phenomenon is challenging because forests are vast, long-lived ecosystems. We develop a novel cloud computing approach to consistently quantify forest structural variability and fire severity across >30 years and nearly 1,000 wildfires in California's Sierra Nevada. We find that greater small-scale structural variability increases resilience by reducing rates of fire-induced tree mortality. Resilience of these forests is likely compromised by structural homogenization from a century of fire suppression, but may be restored with management that increases structural variability of vegetation.

Introduction

Biological systems comprising heterogeneous elements can retain their fundamental properties in the face of regular disturbance. This ability of a heterogeneous system to absorb disturbances, reorganize, and to persist within a domain of stability with respect to its identity, structure, function, and feedbacks is termed resilience (1, 2). Resilience has been demonstrated in complex biological systems characterized by a variety of different types of "heterogeneity" including genetic diversity (3–5), species diversity (6–8), functional diversity (9), topoclimatic complexity (10, 11), and temporal environmental variation (12). An emerging paradigm in forest ecology is that resilience to disturbances such as wildfire and insect outbreaks may arise from spatial variability in the structure of vegetation (13–15).

In much of the western United States, forests are experiencing "unhealthy" conditions which compromise their resilience and leaves them prone to catastrophic shifts in ecosystem type (16). Warmer temperatures coupled with recurrent drought (i.e., "hotter droughts") exacerbate water stress on trees (16–18) and a century of fire suppression has drastically increased forest density and structural homogeneity (19, 20). Combined, these changes are liable to upset the feedbacks between forest structure and pattern-forming ecological disturbances that historically stabilized the system and made it resilient. In the yellow pine/mixed-conifer forests of California's Sierra Nevada mountain range, wildfires kill much larger contiguous patches of trees than in the several centuries prior to Euroamerican settlement making natural forest regeneration after these megafires uncertain (19–22). Forests are essential components of the biosphere with high management priority given their large carbon stores and other valued ecosystem services (16, 23–25), making it critical to understand how and at what scale spatial structural variability affects forest resilience to disturbance.

Resilience of forest ecosystems is fundamentally challenging to quantify because forests comprise long-lived species, span large geographic extents, and are affected by disturbances at a broad range of spatial scales. The ease or difficulty with which a disturbance changes a system's state is termed resistance, and it is a key component of resilience (2) (though some treatments in forest ecology define "resistance" as a distinct process from "resilience"; see (26)). To assess a forest's resistance, the relevant state change to measure is the loss of its characteristic native biota– overstory trees (27). Using this framework, a forest system that is resistant to wildfire should generally experience less overstory tree mortality when a fire occurs.

Wildfire behavior is inherently complex and is influenced by local weather, topography, and fuel conditions created by a legacy of disturbances at any particular place (28). For instance, high surface fuel loads and presence of "ladder fuels" in the understory increase the probability of "crowning" fire behavior, which kills a high proportion of trees (13, 29). A structurally variable forest can largely avoid overstory tree mortality because discontinuous fuel loads interrupt crown fire spread, reduced amounts of accumulated ladder fuel decreases the probability of crowning, and because small tree clumps with fewer trees don't facilitate self-propagating fire behavior (30, 31). In fire-prone forests with relatively intact fire regimes and high structural variability such as in the Jeffrey pine/mixed-conifer forests of the Sierra San Pedro Mártir in Baja, California, there tends to be reduced vegetation mortality after wildfires compared to fire-suppressed forests (13). Thus, more structurally variable forests are predicted to persist due to their resistance to inevitable wildfire disturbance (13, 30, 32). However, it has been difficult to test this foundational concept at broad spatial extents, or resolve at what scale variability in forest structure is meaningful for resilience (33).

Wildfire severity typically describes the proportion of vegetation mortality resulting from fire, and can be measured by comparing pre- and postfire satellite imagery for a specific area. This usually requires considerable manual effort for image collation and processing, followed by calibration with field data (21, 34–41). Efforts to measure severity across broad spatial extents, such as the Monitoring Trends in Burn Severity project (42), are motivated by and fulfill management needs in response to individual fires but are unsuitably subjective for characterizing patterns and trends across large numbers of wildfires (43). Automated efforts to remotely assess wildfire have arisen, but they tend to focus on more aggregate measures of wildfire such as whether an area burned or the probability that it burned rather than the severity of the burn (44–47), but see (48, 49). Here, we present a method to automate the measurement of wildfire severity using minimal user inputs: a geometry of interest (a wildfire perimeter or a field plot location) and an alarm date (the date the fire was discovered). This information is readily available in many fire-prone areas (such as California, via the Fire and Resource Assessment Program; http://frap.fire.ca.gov/projects/fire_data/fire_perimeters_index) or could be derived using existing products (such as the Landsat Burned Area Essential Climate Variable product described in (47)).

Vegetation characteristics can be measured using remotely-sensed imagery (50–52). Texture analysis of these vegetation characteristics can quantify ecologically relevant local environmental heterogeneity across broad spatial extents (53–56), which may be used as a direct measure of ecosystem resilience (57). Developed for image classification and computer vision, texture analysis characterizes each pixel in an image by a summary statistic of its neighboring pixels, and represents a measure of local heterogeneity which itself varies across the landscape (58). Texture analysis of forested areas detects heterogeneity of overstory vegetation, which corresponds to fuel loading and continuity, capturing the primary influence of vegetation structure on fire behavior.

We use freely-available Landsat satellite data and a new image processing approach to calculate wildfire severity for nearly 1,000 wildfires encompassing a wide size range (down to 4 hectares) and long time series

(1984 to 2017) of Sierra Nevada wildfires that burned in yellow pine/mixed-conifer forest. The larger fires that comprise most severity databases are often able to grow large only after escaping initial suppression efforts and burning under extreme fuel and weather conditions (59). We better represent non-extreme fire behavior by measuring severity across a wider range of fire sizes, allowing us to characterize general features of wildfire behavior in this system without bias. We calibrate 56 configurations of our algorithmic approach to ground-based wildfire severity measurements, and select the best performing severity metric to generate a comprehensive, system-wide severity dataset. We pair the resulting extensive database of wildfire severity measures with image texture analysis of vegetation to ask: (1) Does spatial variability in forest structure increase the resilience of California yellow pine/mixed-conifer forests by reducing the severity of wildfires? (2) At what scale does structural variability have the strongest association with wildfire severity? and (3) Does the influence of structural variability on fire severity depend on topography, regional climate, or other conditions?

Results

We found that the remotely sensed relative burn ratio (RBR) metric of wildfire severity measured across a 48-day interval prior to the wildfire discovery date correlated best with ground-based composite burn index (CBI) measurements of severity (5-fold cross validation $R^2 = 0.82$; Fig. 1; Supp. Table 1). Our method to calculate remotely sensed severity using automated Landsat image fetching performs as well or better than most other reported methods that use hand-curation of Landsat imagery (see review in (40)). Further, several combinations of remotely sensed severity metrics, time windows, and interpolation methods validate well with the ground-based severity metrics, including those based on NDVI which is calculated using reflectance in shorter wavelengths than those typically used for measuring severity (Fig. 1). The top three configurations of our remotely sensed severity metric are depicted in Fig. 1.

Based on these model comparisons, we used the relative burn ratio (RBR) calculated using a 48-day time window before the fire and bicubic interpolation as our metric of severity. We created the boolean response variable representing whether the sampled point burned at high-severity or not by determining whether the RBR exceeded 0.282, the threshold for high-severity derived using the non-linear relationship in Eq. 1 (Fig. 1).

Neighborhood size effect

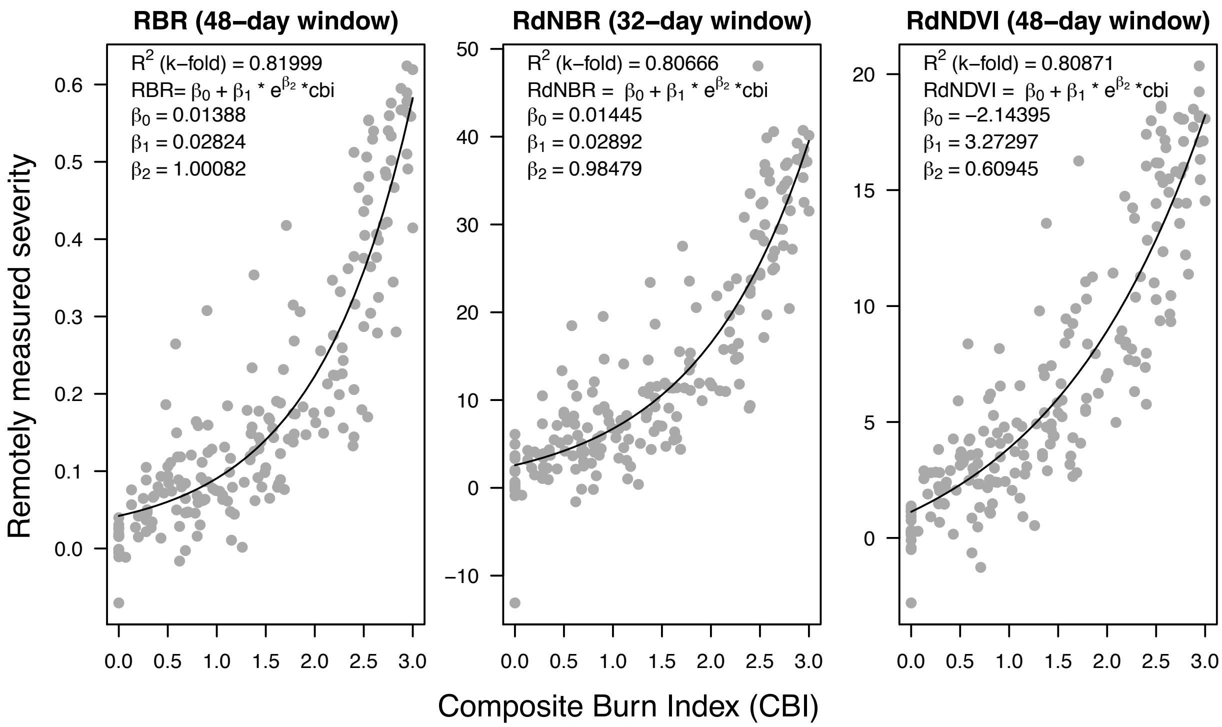

Figure 1: Three top performing remotely-sensed severity metrics based on 5-fold cross validation (relative burn ratio, 48-day window, bicubic interpolation; relative delta normalized burn ratio, 32-day window, bilinear interpolation; and relative delta normalized difference vegetation index, 48-day window, bilinear interpolation) calculated using new automated image collation algorithms, calibrated to 208 field measures of fire severity (composite burn index). See Supplemental Table 1 for performance of all tested models.

Table 1: Comparison of four models described in Eq. 2 using different neighborhood sizes for calculating forest structural variability (standard deviation of NDVI within the neighborhood), neighborhood mean NDVI, and topographic roughness. LOO is a measure of a model's predictive accuracy (with lower values corresponding to more accurate prediction) and is calculated as -2 times the expected log pointwise predictive density (elpd) for a new dataset (60). ΔLOO is the difference between a model's LOO and the lowest LOO in a set of models (i.e., the model with the best predictive accuracy). The Bayesian R^2 is a "data-based estimate of the proportion of variance explained for new data" (61). Note that Bayesian R^2 values are conditional on the model so shouldn't be compared across models, though they can be informative about a single model at a time.

Model	Neighborhood size for variability measure	LOO (-2*elpd)	ΔLOO to best model	SE of ΔLOO	LOO model weight (%)	Bayesian R^2
1	90m x 90m	40785.77	0.000	NA	100	0.299
2	150m x 150m	40841.80	56.029	14.689	0	0.298
3	210m x 210m	40882.65	96.872	20.943	0	0.297
4	270m x 270m	40911.68	125.906	24.731	0	0.297

The model with the best out-of-sample prediction accuracy assessed by leave-one-out cross validation was the model fit using the smallest neighborhood size for the variability of forest structure (standard deviation of neighborhood NDVI), the mean of neighborhood NDVI, and the terrain roughness (standard deviation of elevation) (Tab. 1). Model weighting based on the LOO score suggests 100% of the model weight belongs to the model using the smallest neighborhood size window.

Effects of prefire vegetation density, 100-hour fuel moisture, potential annual heat load, and topographic roughness on wildfire severity

We report the results from fitting the model described in Eq. 2 using the smallest neighborhood size (90m x 90m) because this was the best performing model (see above) and because the size and magnitude of estimated coefficients were similar across neighborhood sizes (Supp. Table 2).

We found that the strongest influence on the probability of a forested area burning at high-severity was the density of the vegetation, as measured by the prefire NDVI at that central pixel. A greater prefire NDVI led to a greater probability of high-severity fire ($\beta_{\text{prefire\_ndvi}} = 1.044$; 95% CI: [0.911, 1.174]); Fig. 2). There was a strong negative relationship between 100-hour fuel moisture and wildfire severity such that increasing 100-hour fuel moisture was associated with a reduction in the probability of a high-severity wildfire ($\beta_{\text{fm100}} =$ -0.569; 95% CI: [-0.71, -0.423]) (Fig. 2). Potential annual heat load, which integrates aspect, slope, and

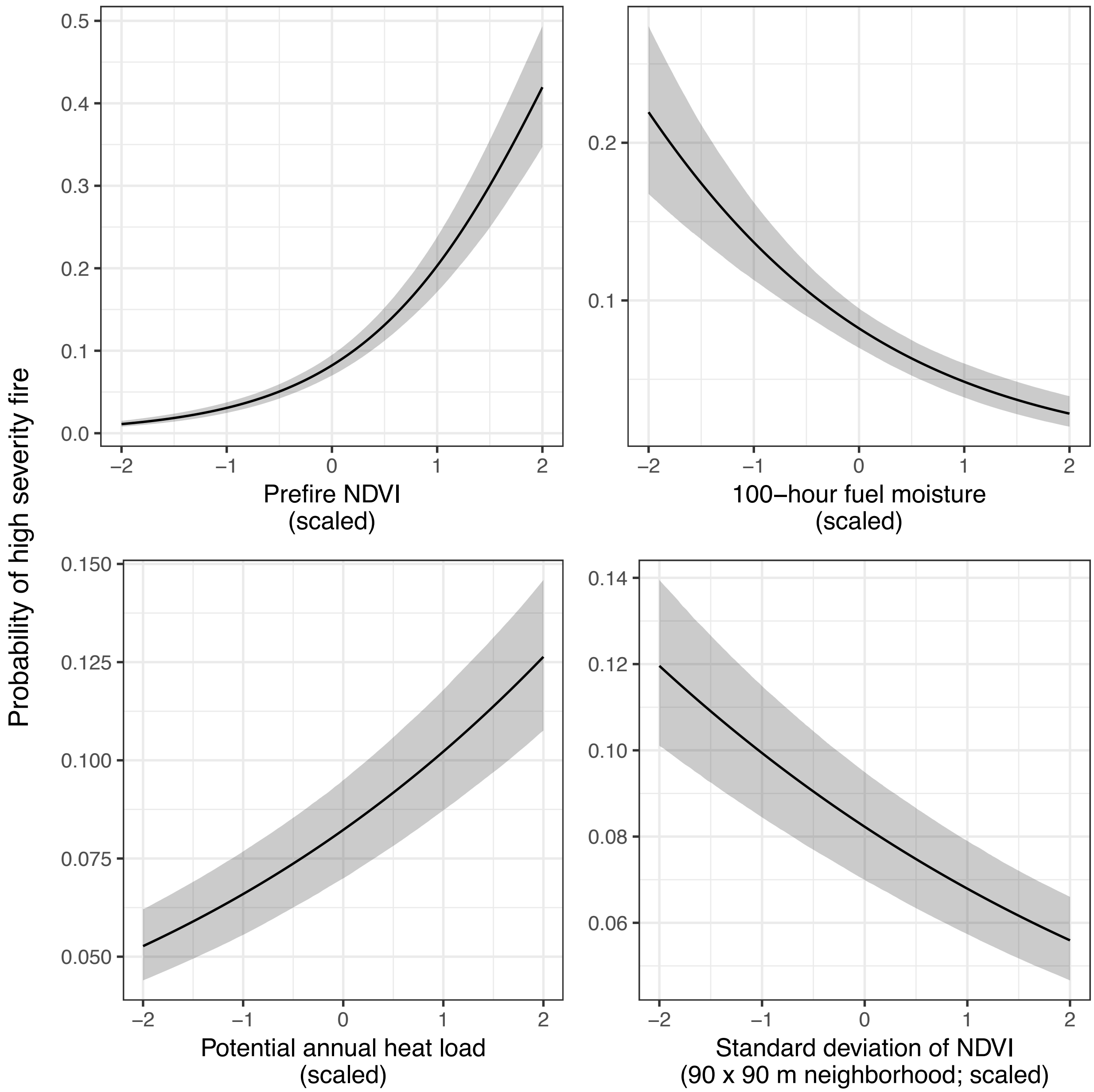

Figure 2: The main effects and 95% credible intervals of the covariates having the strongest relationships with the probability of high-severity fire. All depicted relationships derive from the model using the 90m x 90m neighborhood size window for neighborhood standard deviation of NDVI, neighborhood mean of NDVI, and topographic roughness, as this was the best performing model of the four neighborhood sizes tested. The effect sizes of these covariates were similar for each neighborhood size tested.

latitude, also had a strong positive relationship with the probability of a high-severity fire. Areas that were located on southwest facing sloped terrain at lower latitudes had the highest potential annual heat load, and they were more likely to burn at high-severity (β_{pahl} = 0.239; 95% CI: [0.208, 0.271]) Fig. 2). We found no effect of local topographic roughness on wildfire severity ($\beta_{\text{topographic\_roughness}}$ = -0.01; 95% CI: [-0.042, 0.022]). We found a negative effect of the prefire neighborhood mean NDVI on the probability of a pixel burning at high-severity ($\beta_{\text{nbhd\_mean\_NDVI}}$ = -0.14; 95% CI: [-0.278, 0.002]). This is in contrast to the positive effect of the prefire NDVI of the pixel itself.

There was also a strong negative interaction between the neighborhood mean NDVI and the prefire NDVI of the central pixel ($\beta_{\text{nbhd\_mean\_NDVI*prefire\_NDVI}}$ -0.573; 95% CI: [-0.62, -0.526]).

Effect of variability of vegetation structure on wildfire severity

We found strong evidence for a negative effect of variability of vegetation structure on the probability of a high-severity wildfire ($\beta_{\text{nbhd\_stdev\_NDVI}}$ = -0.208; 95% CI: [-0.247, -0.17]); Fig. 2). We also found significant interactions between variability of vegetation structure and prefire NDVI $\beta_{\text{nbhd\_stdev\_NDVI*prefire\_NDVI}}$ = 0.125; 95% CI: [0.029, 0.218]) as well as between variability of vegetation structure and neighborhood mean NDVI ($\beta_{\text{nbhd\_stdev\_NDVI*nbhd\_mean\_NDVI}}$ = -0.129; 95% CI: [-0.223, -0.034]).

Discussion

Broad-extent, fine-grain, spatially-explicit analyses of whole ecosystems are key to illuminating macroecological phenomena (62). We used a powerful, cloud-based geographic information system and data repository, Google Earth Engine, as a 'macroscope' (63) to study feedbacks between vegetation structure and wildfire disturbance in yellow pine/mixed-conifer forests of California's Sierra Nevada mountain range. With this approach, we reveal and quantify general features of this forest system, and gain deeper insights into the mechanisms underlying its function.

Factors influencing the probability of high-severity wildfire

We found that the strongest influence on the probability of high-severity wildfire was prefire NDVI. Greater NDVI corresponds to high canopy cover and vegetation density (50) which translate directly to live fuel loads in the forest canopy and can increase high severity fire (49). Critically, overstory canopy cover and density also correlate with surface fuel loads (64, 65), which play a larger role in driving high severity fire compared to canopy fuel loads in these forests (66). Thus NDVI is likely a strong predictor of fire severity because it is correlated with both surface fuel loads and canopy live fuel density.

We found a strong positive effect of potential annual heat load as well as a strong negative effect of 100-hour fuel moisture, results which corroborates similar studies (67). Some work has shown that terrain ruggedness (68), and particularly coarser-scale terrain ruggedness (69), is an important predictor of wildfire severity, but we found no effect using our measure of terrain ruggedness.

Critically, we found a strong negative effect of forest structural variability on wildfire severity that was opposite in direction but similar in magnitude to the effect of potential annual heat load. Just as the positive effect of NDVI is likely driven by surface fuel loads, the negative effect of variability in NDVI (our measure of structural variability), is likely driven by discontinuity in surface fuel loads, which can reduce the probability of initiation and spread of tree-killing crown fires (29, 30, 70, 71).

Feedback between forest structural variability and wildfire severity

This system-wide inverse relationship between structural variability and wildfire severity closes a feedback that links past and future fire behavior via forest structure. Frequent, mixed-severity wildfire generates variable forest structure (14, 72, 73), which in turn, as we demonstrate, dampens the severity of future fire. In contrast, exclusion of wildfire homogenizes forest structure and increases the probability that a fire, when it occurs, will produce large, contiguous patches of overstory mortality (19, 22). The proportion and spatial configuration of fire severity in fire-prone forests are key determinants of their long-term persistence (19, 22). Lower-severity fire or scattered patches of higher-severity fire reduce the risk of conversion to a non-forest vegetation type (19, 74), while prospects for forest regeneration are bleak when high-severity patch sizes are much larger than the natural range of variation for the system (16, 19, 20, 75–78). Thus, the forest-structure-mediated feedback between past and future fire severity underlies the resilience of the Sierra Nevada yellow pine/mixed-conifer system.

Neighborhood size

We found that the effect of a forest patch's neighborhood characteristics on the probability of high-severity fire was strongest at the smallest neighborhood size that we tested, 90m x 90m. This suggests that the moderating effect of variability in vegetation structure on fire severity is a very local phenomenon. This corroborates work by (79), who found that crown fires (with high tree killing potential) were almost always reduced to surface fires (with low tree killing potential) within 70m of entering an fuel reduction treatment area.

At a landscape level, forest treatments that reduce fuel loads and increase structural variability can be effective at reducing fire severity across broader spatial scales (80). This may reflect that severity patterns for a whole fire are an emergent property of very local interactions between forest structure and fire behavior. Some work suggests that the scale of these interactions may depend on even broader-scale effects of fire weather, with small-scale variability failing to influence fire behavior under extreme conditions (81, 82), though we did not detect such an interaction. The notion of emergent patterns of severity arising from local effects of vegetation structure is supported by work on fuel reduction treatments, which suggests that fire behavior can be readily modified with forest structural changes to only 20% (when strategically located) to 60% (when randomly located) of the landscape (30).

Correlation between covariates and interactions

Unexpectedly, we found a strong interaction between the prefire NDVI at a pixel and its neighborhood mean NDVI. These two variables are strongly correlated (Spearman's ρ = 0.97), so the general effect of this interaction is to dampen the dominating effect of prefire NDVI. Thus, though the marginal effect of prefire NDVI on the probability of high-severity fire is still positive and large, its real-world effect might be more comparable to other modeled covariates when including the negative main effect of neighborhood mean NDVI, the negative interaction effect of prefire NDVI and neighborhood mean NDVI, and their tendency to covary (compare the real-world effect of vegetation density: $\beta_{\text{prefire\_ndvi}} + \beta_{\text{nbhd\_mean\_NDVI}} + \beta_{\text{nbhd\_mean\_NDVI*prefire\_NDVI}} = 0.331$, to the effect of 100-hour fuel moisture, which becomes the effect with the greatest magnitude: β_{fm100} = -0.569).

In the few cases when prefire NDVI and the neighborhood mean NDVI contrast, there is an overall effect of increasing the probability of high-severity fire. When prefire NDVI at the central pixel is high and the neighborhood NDVI is low (e.g., an isolated vegetation patch; Supplemental Fig. 2), the probability of high-severity fire is expected to dramatically increase. When prefire NDVI at the central pixel is low and the neighborhood NDVI is high (e.g., a hole in the center of an otherwise dense forest; Supplemental Fig. 2), the probability of high-severity fire at that central pixel is still expected to be fairly high even though there is limited vegetation density (see Supplemental Fig. 2). In these forest NDVI datasets, when these variables do decouple, they tend to do so in the “hole in the forest” case and lead to a greater probability of high-severity fire at the central pixel despite the lower vegetation density there. This can perhaps be explained if the consistently high vegetation density in a local neighborhood– itself more likely to burn at high-severity– exerts a contagious effect on the central pixel, raising its probability of burning at high-severity regardless of how much fuel might be there to burn.

A new approach to remotely sensing wildfire severity

We developed a new approach to calculating wildfire severity leveraging the cloud-based data catalog, the large parallel processing system, and the distribution of computation tasks in Google Earth Engine to enable rapid high-throughput analyses of earth observation data (83). Our programmatic assessment of wildfire severity across the 979 Sierra Nevada yellow pine/mixed-conifer fires in the FRAP perimeter database, which required fetching thousands of Landsat images and performing dozens of calculations across them, was automated and took less than an hour to complete. We found that the relative burn ratio (RBR) calculated using prefire Landsat images collected over a 48-day period prior to the fire and postfire Landsat images collected over a 48-day period one year after the prefire images validated the best with ground-based severity measurements (composite burn index; CBI). Further, we found that this method was robust to a wide range of severity metrics, time windows, and interpolation techniques.

Most efforts to calculate severity from satellite data rely on hand curation of a single prefire and a single postfire image (21, 34–41). Recently, (49) found that using a composite of several prefire images and several postfire images to detect fire impacts performed at least as well as using a single pre- and postfire image. Using composite images also facilitated automated image fetching. (49) used 3- to 4-month windows during pre-specified times of the year (depending on the fire's region) to collate pre- and postfire imagery one year before the fire and one year after. In contrast, we tested multiple time window lengths based on the fire start date regardless of when it burned during the year. Basing our pre- and postfire image fetching on fixed lengths of time since the fire start date standardized the amount of time elapsed in each severity assessment. Our best remotely sensed severity configuration used a much shorter time window compared to (49) (48 days versus 3 to 4 months), which likely balanced an incorporation of enough imagery to be representative of the pre- and postfire vegetation conditions but not so many images that different phenological conditions across the time window added noise to each composite.

Many algorithms have been developed to measure fire effects on vegetation in an attempt to better correspond to field data (21, 38, 84). We found that several other remotely sensed measures of severity, including one based on NDVI that is rarely deployed, validated nearly as well with ground-based data as the best configuration (RBR calculated using a 48-day time window). We echo the conclusion of (85) that the validation of differences between pre- and postfire NDVI to field measured severity data, which uses near infrared reflectance, is comparable to validation using more commonly used severity metrics (e.g., RdNBR and RBR) that rely on short wave infrared reflectance. One immediately operational implication of this is that the increasing availability of low-cost small unhumanned aerial systems (sUAS a.k.a. drones) and near-infrared-detecting imagers (e.g., those used for agriculture monitoring) may be used to reliably measure wildfire severity at very high spatial resolutions.

Conclusions

While the severity of a wildfire in any given place is controlled by many variables, we have presented strong evidence that, across large areas of forest, variable forest structure generally makes yellow pine/mixed-conifer forest in the Sierra Nevada more resistant to this inevitable disturbance. It has been well-documented that frequent, low-severity wildfire maintains forest structural variability. Here, we demonstrate a system-wide reciprocal effect suggesting that greater local-scale variability of vegetation structure makes fire-prone, dry forests more resilient to wildfire and may increase the probability of their long-term persistence.

Material and Methods

Study system

Our study assesses the effect of vegetation structure on wildfire severity in the Sierra Nevada mountain range of California in yellow pine/mixed-conifer forests (Fig. 3). This system is dominated by a mixture of conifer species including ponderosa pine (*Pinus ponderosa*), sugar pine (*Pinus lambertiana*), incense-cedar (*Calocedrus decurrens*), Douglas-fir (*Pseudotsuga menziesii*), white fir (*Abies concolor*), and red fir (*Abies magnifica*), angiosperm trees primarily including black oak (*Quercus kelloggii*), as well as shrubs (20). We considered "yellow pine/mixed-conifer forest" to be all areas designated as a yellow pine, dry mixed-conifer, or moist mixed-conifer pre-settlement fire regime (PFR) in the USFS Fire Return Interval Departure database (https://www.fs.usda.gov/detail/r5/landmanagement/gis/?cid=STELPRDB5327836), which reflects potential vegetation and is less sensitive to recent land cover change (22). We considered the Sierra Nevada region to be the area within the Sierra Nevada Foothills, the High Sierra Nevada, and the Tehachapi Mountain Area Jepson ecoregions (86).

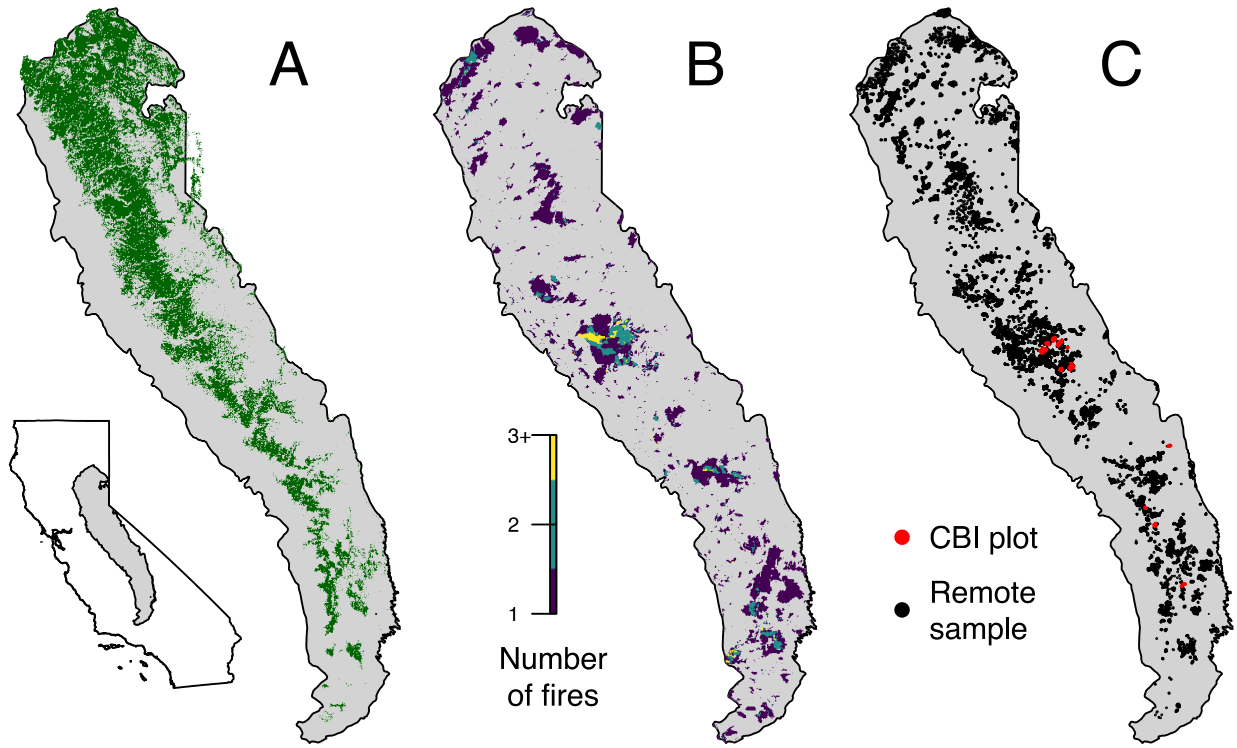

Figure 3: Geographic setting of the study. A) Location of yellow pine/mixed-conifer forests as designated by the Fire Return Interval Departure (FRID) product which, among other things, describes the potential vegetation in an area based on the pre-Euroamerican settlement fire regime. B) Locations of all fires covering greater than 4 hectares that burned in yellow pine/mixed-conifer forest between 1984 and 2017 in the Sierra Nevada mountain range of California according to the State of California Fire Resource and Assessment Program database, the most comprehensive database of fire perimeters of its kind. Colors indicate how many fire perimeters overlapped a given pixel within the study time period. C) (red) Locations of 208 composite burn index (CBI) ground plots used to calibrate the remotely sensed measures of severity. (black) Locations of random samples drawn from 979 unique fires depicted in panel B that were in yellow pine/mixed-conifer forest as depicted in panel A, and which were designated as "burned" by exceeding a threshold relative burn ratio (RBR) determined by calibrating the algorithm presented in this study with ground-based CBI measurements.

A new approach to remotely sensing wildfire severity

We measured forest vegetation characteristics and wildfire severity using imagery from the Landsat series of satellites (21, 42) with radiometric correction post-processing (87–90). Landsat satellites image the entire Earth approximately every 16 days with a 30m pixel resolution. We used Google Earth Engine, a massively parallel cloud-based geographic information system and image hosting platform, for all image collation and processing (83).

We calculated wildfire severity for the most comprehensive digital record of fire perimeters in California: The California Department of Forestry and Fire Protection, Fire and Resource Assessment Program (FRAP) fire perimeter database (http://frap.fire.ca.gov/projects/fire_data/fire_perimeters_index). The FRAP database includes all known fires that covered more than 4 hectares, compared to the current standard severity database in this region which only includes fires covering greater than 80 hectares (21, 22, 91, 92). Using the FRAP database of fire perimeters, we quantified fire severity within each perimeter of 979 wildfires in the Sierra Nevada yellow pine/mixed-conifer forest that burned between 1984 and 2017. Our approach more than doubles the number of fire events represented from 430 to 979, though only increases the total burned area represented from 7.44e+05 to 7.67e+05 hectares because most of the additional fires are small. We use a consistent algorithmic approach to calculate fire severity across all fires, avoiding subjective judgements that some previous approaches have used to characterize severity separately for each fire.

Fetching and processing pre- and postfire imagery

For each fire perimeter, we fetched a time series of prefire Landsat images starting the day before the fire alarm date and extending backward in time by a user-defined time window. An analogous postfire time series of Landsat imagery was fetched exactly one year after the date range used to filter the prefire collection. We tested 4 time windows: 16, 32, 48, or 64 days which were chosen to ensure that at least 1, 2, 3, or 4 Landsat images were captured by the date ranges (Supplemental Fig. 1). The Landsat archive we filtered included imagery from Landsat 4, 5, 7, and 8, so each pre- and postfire image collection may contain a mix of scenes from different satellite sources to enhance coverage. For each image in the pre- and postfire image collections, we masked pixels that were not clear (i.e., clouds, cloud shadows, snow, and water) using the CFMask algorithm (93).

For each Landsat image in the prefire and postfire collections, we calculated standard indices that capture vegetation cover and fire effects such as charring. Normalized difference vegetation index (NDVI) correlates with vegetation density, canopy cover, and leaf area index (50). Normalized burn ratio (NBR) and normalized burn ratio version 2 (NBR2) respond strongly to fire effects on vegetation (47, 84, 89, 90, 94) (Equations in Supplemental Methods).

We composited each prefire image collection (including the pixel values representing NDVI, NBR, and NBR2) into a single prefire image and each postfire image collection into a single postfire image, by calculating the median of the unmasked values on a per-pixel basis across the stack of images in each pre- and postfire collection. Composite pre- and postfire images can be successfully used to measure wildfire severity instead of using raw, individual images (49).

We composited each pre- and postfire image collection (including the pixel values representing NDVI, NBR, and NBR2) into a single pre- and postfire image using a median reducer, which calculated the median of the unmasked values on a per-pixel basis across the stack of images in each collection. Composite pre- and postfire images can be successfully used to measure wildfire severity instead of using raw, individual images (49).

Calculating wildfire severity

Using the compositing approach, we calculated the most commonly used metrics of remotely-sensed wildfire severity to validate against ground-based data: the relative burn ratio (RBR) (38), the delta normalized burn ratio (dNBR) (21, 42), the relative delta normalized burn ratio (RdNBR) (21, 92), the delta normalized burn ratio 2 (dNBR2) (47), the relative delta normalized burn ratio 2 (RdNBR2), and the delta normalized difference vegetation index (dNDVI) (42). We also calculate a new, analogous metric to the RdNBR using NDVI– the relative delta normalized difference vegetation index (RdNDVI). We calculated the delta severity indices (dNBR, dNBR2, dNDVI) without multiplying by a rescaling constant (e.g., we did not multiply the result by 1000 as in (21)). Following (48), we did not correct the delta indices using a phenological offset value, as our approach implicitly accounts for phenology by incorporating multiple cloud-free images across the same time window both before the fire and one year later. (Full equations can be found in the Supplemental Methods)

Example algorithm outputs are shown in Fig. 4.

Calibrating remotely-sensed wildfire severity with field-measured wildfire severity

We calibrated our remotely-sensed measure of wildfire severity with 208 field measures of overstory tree mortality from two previously published studies (85, 95) (Fig. 3). The Composite Burn Index (CBI) is a

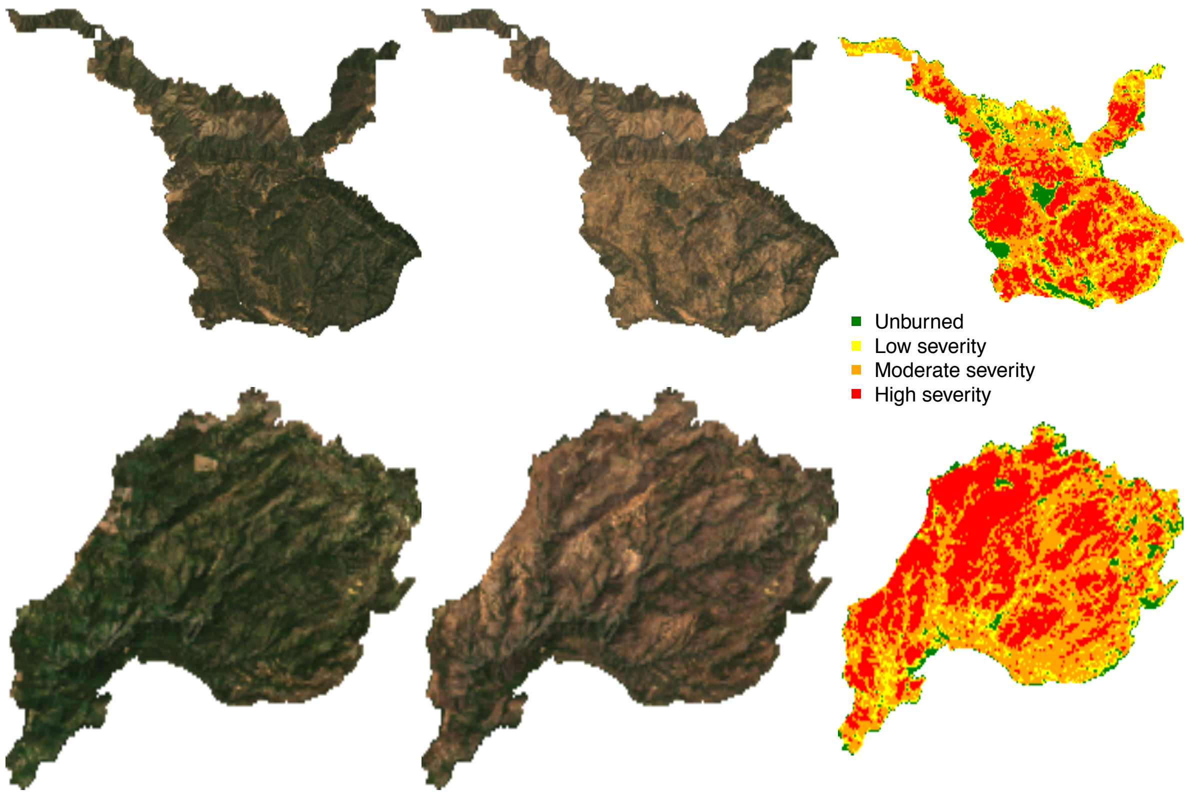

Figure 4: Example algorithm outputs for the Hamm Fire of 1987 (top half) and the American Fire of 2013 (bottom half) showing: prefire true color image (left third), postfire true color image (center third), relative burn ratio (RBR) calculation using a 48-day image collation window before the fire and one year later (right third). For visualization purposes, these algorithm outputs have been resampled to a resolution of 100m x 100m from their original resolution of 30m x 30m. Data used for analyses were sampled from the outputs at the original resolution.

metric of vegetation mortality across several vertical vegetation strata within a 30m diameter field plot (84). The CBI ranges from 0 (no fire impacts) to 3 (very high fire impacts), and has a long history of use as a standard for calibrating remotely-sensed severity data (21, 34, 36, 38, 39, 49, 84). Following (21), (34), (38), and (49), we fit a non-linear model to each remotely-sensed severity metric of the following form:

$$(1)\quad \text{remote\_severity} = \beta_0 + \beta_1 e^{\beta_2 \text{cbi\_overstory}}$$

We fit the model in Eq. 1 for all 7 of our remotely-sensed severity metrics (RBR, dNBR, RdNBR, dNBR2, RdNBR2, dNDVI, RdNDVI) using 4 different time windows from which to collate satellite imagery (16, 32, 48, and 64 days). Following (36), (38), and (49), we used bilinear interpolation to extract remotely-sensed severity at the locations of the CBI field plots to better align remote and field measurements. We also extracted remotely-sensed severity values using bicubic interpolation. In total, we fit 56 models (7 severity measures, 4 time windows, 2 interpolation methods) and performed five-fold cross validation using the `modelr` and `purrr` packages in R (96–98). To compare goodness of model fits with (21), (34), and (38), we report the average R^2 value from the five folds for each of the 56 models.

Remote sensing other conditions

Vegetation structural variability

We used texture analysis to calculate a remotely-sensed measure of local forest variability (56, 58). Within a moving square neighborhood window with sides of 90m, 150m, 210m, and 270m, we calculated forest variability for each pixel as the standard deviation of the NDVI values of its neighbors (not including itself). NDVI correlates well with foliar biomass, leaf area index, and vegetation cover (50), so a higher standard deviation of NDVI within a given local neighborhood corresponds to discontinuous canopy cover and abrupt vegetation edges (see Fig. 5) (99). Canopy cover is positively correlated with surface fuel loads including dead and down wood, grasses, and short shrubs (64, 65), which are primarily responsible for initiation and spread of “crowning” fire behavior which kills overstory trees (66).

Topographic conditions

Elevation data were sourced from the Shuttle Radar Topography Mission (100), a 1-arc second digital elevation model. Slope and aspect were extracted from the digital elevation model. Per-pixel topographic roughness was calculated as the standard deviation of elevation values within the same-sized kernels as those used for variability in forest structure (90m, 150m, 210m, and 270m on a side and not including the central pixel).

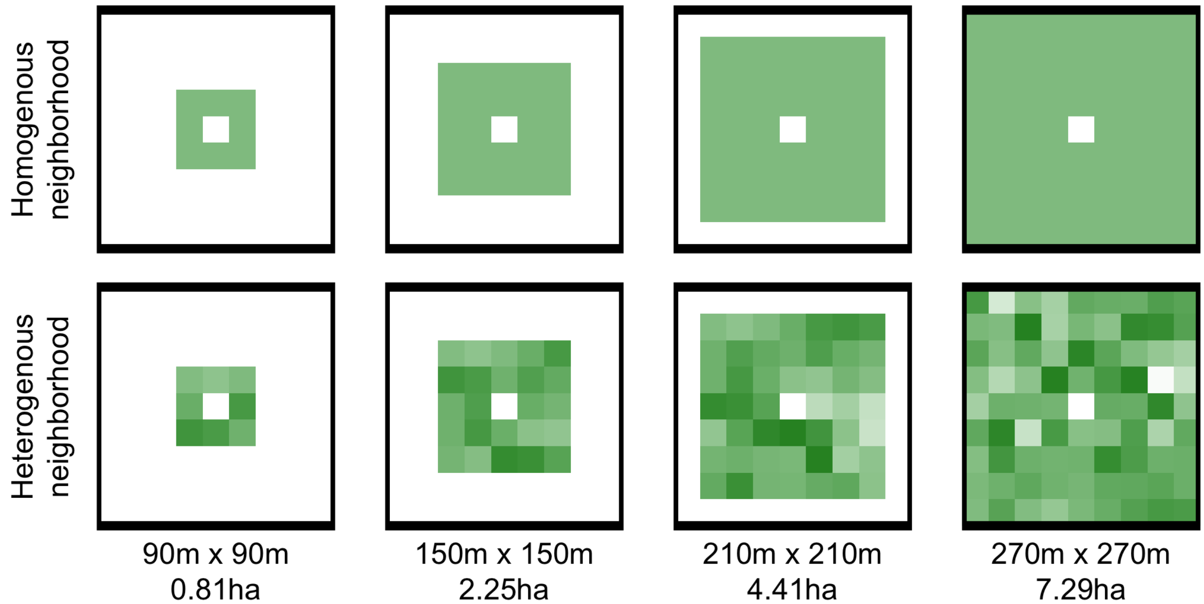

Figure 5: Example of homogenous forest (top row) and heterogenous forest (bottom row) with the same mean NDVI values (~0.6). Each column represents forest structural variability measured using a different neighborhood size.

We used the digital elevation model to calculate the potential annual heat load at each pixel, which is an integrated measure of latitude, slope, and a folding transformation of aspect about the northeast-southwest line ((101) with correction in (102); See Supplemental Methods for equations)

Moisture conditions

The modeled 100-hour fuel moisture data were sourced from the gridMET product, a gridded meteorological product with a daily temporal resolution and a 4km x 4km spatial resolution (103). We calculated 100-hour fuel moisture as the median 100-hour fuel moisture for the 3 days prior to the fire. The 100-hour fuel moisture is a correlate of the regional temperature and moisture which integrates the relative humidity, the length of day, and the amount of precipitation in the previous 24 hours. Thus, this measure is sensitive to multiple hot dry days across the 4km x 4km spatial extent of each grid cell, but not to diurnal variation in relative humidity nor to extreme weather events during a fire.

Remote samples

Approximately 100 random points were selected within each FRAP fire perimeter in areas designated as yellow pine/mixed-conifer forest and the values of wildfire severity as well as the values of each covariate were extracted at those points using nearest neighbor interpolation. Using the calibration equation described in Eq. 1 for the best configuration of the remote severity metric, we removed sampled points corresponding to "unburned" area prior to analysis (i.e., below an RBR threshold of 0.045). The random sampling amounted to 54409 total samples across 979 fires.

Modeling the effect of forest variability on severity

We used the Relative Burn Ratio (RBR) calculated using bicubic interpolation within a 48-day window to derive our response variable for analyses of forest structural variability, as it showed the best correspondence to field severity data measured as average R^2 in the 5-fold cross validation. Using the non-linear relationship between RBR and CBI from the best performing calibration model, we calculated the threshold RBR corresponding to "high-severity" signifying complete or near-complete overstory mortality (RBR value of 0.282 corresponding to a CBI value of 2.25). If the severity at a remote sample point was greater than this threshold, the point was scored as a 1. We used a hierarchical logistic regression model (Eq. 2) to assess the probability of high-severity wildfire as a linear combination of the remote metrics described above: prefire NDVI of each pixel, standard deviation of NDVI within a neighborhood (i.e., forest structural variability), the mean NDVI within a neighborhood, 100-hour fuel moisture, potential annual heat load, and topographic roughness. We included two-way interactions between the structural variability measure and prefire NDVI, neighborhood mean NDVI, and 100-hour fuel moisture. We include the two-way interaction between a pixel's prefire NDVI and its neighborhood mean NDVI to account for structural variability that may arise from differences between these variables (see Supplemental Fig. 2). We scaled all predictor variables, used weakly-regularizing priors, and estimated an intercept for each individual fire with pooled variance.

$$
\begin{aligned}
severity_{i,j} &\sim Bern(\phi_{i,j}) \\
(2) \quad logit(\phi_{i,j}) &= \beta_0 + \\
&\beta_{\text{nbhd\_stdev\_NDVI}} * \text{nbhd\_stdev\_NDVI}_i + \\
&\beta_{\text{prefire\_NDVI}} * \text{prefire\_NDVI}_i + \\
&\beta_{\text{nbhd\_mean\_NDVI}} * \text{nbhd\_mean\_NDVI}_i + \\
&\beta_{\text{fm100}} * \text{fm100}_i + \\
&\beta_{\text{pahl}} * \text{pahl}_i + \\
&\beta_{\text{topographic\_roughness}} * \text{topographic\_roughness}_i + \\
&\beta_{\text{nbhd\_stdev\_NDVI*fm100}} * \text{nbhd\_stdev\_NDVI}_i * \text{fm100}_i + \\
&\beta_{\text{nbhd\_stdev\_NDVI*prefire\_NDVI}} * \text{nbhd\_stdev\_NDVI}_i * \text{prefire\_NDVI}_i + \\
&\beta_{\text{nbhd\_stdev\_NDVI*nbhd\_mean\_NDVI}} * \text{nbhd\_stdev\_NDVI}_i * \text{nbhd\_mean\_NDVI}_i + \\
&\beta_{\text{nbhd\_mean\_NDVI*prefire\_NDVI}} * \text{nbhd\_mean\_NDVI}_i * \text{prefire\_NDVI}_i + \\
&\gamma_j \\
\gamma_j &\sim \mathcal{N}(0, \sigma_{\text{fire}})
\end{aligned}
$$

Assessing the relevant scale of forest variability

Each neighborhood size (90m, 150m, 210m, 270m on a side) was substituted in turn for the neighborhood standard deviation of NDVI, neighborhood mean NDVI, and terrain ruggedness covariates to generate a candidate set of 4 models. To assess the scale at which the forest structure variability effect manifests, we compared the 4 candidate models based on different neighborhood sizes using leave-one-out cross validation (LOO cross validation) (60). We inferred that the neighborhood size window used in the best-performing model reflected the scale at which the forest structure variability effect had the most support.

Statistical software

We used `R` for all statistical analyses (98). We used the `brms` package to fit mixed effects models in a Bayesian framework which implements the No U-Turn Sampler (NUTS) extension to the Hamiltonian Monte Carlo algorithm (104, 105). We used 4 chains with 3000 samples per chain (1500 warmup samples and 1500 posterior samples) and chain convergence was assessed for each estimated parameter by ensuring Rhat values were less than or equal to 1.01 (105).

Data availability

All data and analysis code are available via the Open Science Framework (DOI to be established) including a new dataset representing wildfire severity, vegetation characteristics, and regional climate conditions within the perimeters of 1,090 fires from the FRAP database that burned in yellow pine/mixed-conifer forest in the Sierra Nevada, California between 1984 and 2017.

Acknowledgements

We thank Connie Millar and Derek Young for valuable comments about this work and we also thank the community of Google Earth Engine developers for prompt and helpful insights about the platform. Funding was provided by NSF Graduate Research Fellowship Grant #DGE- 1321845 Amend. 3 (to MJK).

References

1. Holling CS (1973) Resilience and Stability of Ecological Systems. *Annual Review of Ecology and Systematics* 4(1973):1–23.

2. Walker B, Holling CS, Carpenter SR, Kinzig A (2004) Resilience, adaptability, and transformability in social-ecological systems. *Ecology and Society* 9(2):5.

3. Reusch TBH, Ehlers A, Hämmerli A, Worm B (2005) Ecosystem recovery after climatic extremes enhanced by genotypic diversity. *Proceedings of the National Academy of Sciences* 102(8):2826–2831.

4. Baskett ML, Gaines SD, Nisbet RM (2009) Symbiont diversity may help coral reefs survive moderate climate change. *Ecological Applications* 19(1):3–17.

5. Agashe D (2009) The stabilizing effect of intraspecific genetic variation on population dynamics in novel and ancestral habitats. *The American Naturalist* 174(2):255–67.

6. Tilman D (1994) Competition and biodiversity in spatially structured habitats. *Ecology* 75(1):2–16.

7. Chesson P (2000) Mechanisms of maintenance of species diversity. *Annual Review of Ecology and Systematics* 31:343–366.

8. Cadotte M, Albert CH, Walker SC (2013) The ecology of differences: Assessing community assembly with trait and evolutionary distances. *Ecology Letters* 16:1234–1244.

9. Gazol A, Camarero JJ (2016) Functional diversity enhances silver fir growth resilience to an extreme drought. *Journal of Ecology* (2013). doi:10.1111/1365-2745.12575.

10. Ackerly DD, et al. (2010) The geography of climate change: Implications for conservation biogeography. *Diversity and Distributions* 16(3):476–487.

11. Lenoir J, et al. (2013) Local temperatures inferred from plant communities suggest strong spatial buffering of climate warming across Northern Europe. *Global Change Biology* 19:1470–1481.

12. Questad EJ, Foster BL (2008) Coexistence through spatio-temporal heterogeneity and species sorting in grassland plant communities. *Ecology Letters* 11(7):717–726.

13. Stephens SL, Fry DL, Franco-Vizcaíno E (2008) Wildfire and spatial patterns in forests in northwestern Mexico: The United States wishes it had similar fire problems. *Ecology and Society*.

14. North M, Stine P, Hara KO, Zielinski W, Stephens S (2009) An Ecosystem Management Strategy for Sierran Mixed- Conifer Forests. *General Technical Report PSW-GTR-220* (March):1–49.

15. Virah-Sawmy M, Willis KJ, Gillson L (2009) Threshold response of Madagascar's littoral forest to sea-level rise. *Global Ecology and Biogeography* 18:98–110.

16. Millar CI, Stephenson NL (2015) Temperate forest health in an era of emerging megadisturbance. *Science* 349(6250):823–826.

17. Williams AP, et al. (2012) Temperature as a potent driver of regional forest drought stress and tree mortality. *Nature Climate Change* 3(3):292–297.

18. Clark JS, et al. (2016) The impacts of increasing drought on forest dynamics , structure , and biodiversity in the United States. *Global Change Biology* 22:2329–2352.

19. Stevens JT, Collins BM, Miller JD, North MP, Stephens SL (2017) Changing spatial patterns of stand-replacing fire in California conifer forests. *Forest Ecology and Management* 406(June):28–36.

20. Safford HD, Stevens JT (2017) Natural Range of Variation (NRV) for yellow pine and mixed conifer forests in the bioregional assessment area, including the Sierra Nevada, southern Cascades, and Modoc and Inyo National Forests. *Gen Tech Rep PSW-GTR-2562* (October):1–151.

21. Miller JD, Thode AE (2007) Quantifying burn severity in a heterogeneous landscape with a relative version of the delta Normalized Burn Ratio (dNBR). *Remote Sensing of Environment* 109:66–80.

22. Steel ZL, Koontz MJ, Safford HD (2018) The changing landscape of wildfire: Burn pattern trends and implications for California's yellow pine and mixed conifer forests. *Landscape Ecology* 33:1159–1176.

23. Hansen MC, et al. (2013) High-resolution global maps of 21st-century forest cover change. *Science* 342(November):850–853.

24. Crowther TW, et al. (2015) Mapping tree density at a global scale. *Nature* 525:201–205.

25. Trumbore S, Brando P, Hartmann H (2015) Forest health and global change. *Science* 349(6250).

26. Millar CI, Stephenson NL, Stephens SL (2007) Climate change and forests of the future: Managing in the face of uncertainty. *Ecological Applications* 17(8):2145–2151.

27. Keith DA, et al. (2013) Scientific Foundations for an IUCN Red List of Ecosystems. *PLoS ONE* 8(5). doi:10.1371/journal.pone.0062111.

28. Sugihara NG, Barbour MG (2006) Fire and California vegetation. *Fire in California's Ecosystems*, eds Sugihara NG, Van Wagtendonk JW, Shaffer KE, Fites-Kaufman J, Thode AE (University of California Press, Berkeley; Los Angeles, CA, USA), pp 1–9. 1st Ed.

29. Agee JK, Skinner CN (2005) Basic principles of forest fuel reduction treatments. *Forest Ecology and Management* 211(1-2):83–96.

30. Graham RT, McCaffrey S, Jain TB (2004) *Science basis for changing forest structure to modify wildfire behavior and severity* (US Department of Agriculture, Forest Service, Rocky Mountain Research Station, Fort Collins, CO).

31. Scholl AE, Taylor AH (2010) Fire regimes, forest change, and self-organization in an old-growth mixed-conifer forest, Yosemite National Park, USA. *Ecological Applications* 20(2):362–380.

32. Moritz MA, Morais ME, Summerell LA, Carlson JM, Doyle J (2005) Wildfires, complexity, and highly optimized tolerance. *Proceedings of the National Academy of Sciences* 102(50):17912–7.

33. Kotliar NB, Wiens J a (1990) Multiple Scales of Patchiness and Patch Structure: A Hierarchical Framework for the Study of Heterogeneity. *Oikos* 59(2):253–260.

34. Miller JD, et al. (2009) Calibration and validation of the relative differenced Normalized Burn Ratio (RdNBR) to three measures of fire severity in the Sierra Nevada and Klamath Mountains, California, USA. *Remote Sensing of Environment* 113(3):645–656.

35. De Santis A, Asner GP, Vaughan PJ, Knapp DE (2010) Mapping burn severity and burning efficiency in California using simulation models and Landsat imagery. *Remote Sensing of Environment* 114(7):1535–1545.

36. Cansler CA, McKenzie D (2012) How robust are burn severity indices when applied in a new region? Evaluation of alternate field-based and remote-sensing methods. *Remote Sensing* 4(2):456–483.

37. Veraverbeke S, Hook SJ (2013) Evaluating spectral indices and spectral mixture analysis for assessing fire severity, combustion completeness and carbon emissions. *International Journal of Wildland Fire* 22(5):707–720.

38. Parks SA, Dillon GK, Miller C (2014) A new metric for quantifying burn severity: The relativized burn ratio. *Remote Sensing* 6(3):1827–1844.

39. Prichard SJ, Kennedy MC (2014) Fuel treatments and landform modify landscape patterns of burn severity in an extreme fire event. *Ecological Applications* 24(3):571–590.

40. Edwards AC, Russell-Smith J, Maier SW (2018) A comparison and validation of satellite-derived fire severity mapping techniques in fire prone north Australian savannas: Extreme fires and tree stem mortality. *Remote Sensing of Environment* 206(May 2017):287–299.

41. Fernández-García V, et al. (2018) Burn severity metrics in fire-prone pine ecosystems along a climatic gradient using Landsat imagery. *Remote Sensing of Environment* 206(December 2017):205–217.

42. Eidenshink J, et al. (2007) A project for monitoring trends in burn severity. *Fire Ecology* 3(1):3–21.

43. Kolden CA, Smith AMS, Abatzoglou JT (2015) Limitations and utilisation of Monitoring Trends in Burn Severity products for assessing wildfire severity in the USA. *International Journal of Wildland Fire* 24(7):1023–1028.

44. Bastarrika A, Chuvieco E, Martín MP (2011) Mapping burned areas from landsat TM/ETM+ data with a two-phase algorithm: Balancing omission and commission errors. *Remote Sensing of Environment* 115(4):1003–1012.

45. Goodwin NR, Collett LJ (2014) Development of an automated method for mapping fire history captured in Landsat TM and ETM+ time series across Queensland, Australia. *Remote Sensing of Environment* 148:206–221.

46. Boschetti L, Roy DP, Justice CO, Humber ML (2015) MODIS-Landsat fusion for large area 30m burned area mapping. *Remote Sensing of Environment* 161:27–42.

47. Hawbaker TJ, et al. (2017) Mapping burned areas using dense time-series of Landsat data. *Remote Sensing of Environment* 198:504–522.

48. Reilly MJ, et al. (2017) Contemporary patterns of fire extent and severity in forests of the Pacific Northwest, USA (1985-2010). *Ecosphere* 8(3). doi:10.1002/ecs2.1695.

49. Parks S, Holsinger L, Voss M, Loehman R, Robinson N (2018) Mean Composite Fire Severity Metrics

Computed with Google Earth Engine Offer Improved Accuracy and Expanded Mapping Potential. *Remote Sensing* 10(6):879.

50. Rouse JW, Hass RH, Schell J, Deering D (1973) Monitoring vegetation systems in the great plains with ERTS. *Third Earth Resources Technology Satellite (ERTS) symposium* 1:309–317.

51. Asner GP, et al. (2015) Progressive forest canopy water loss during the 2012–2015 California drought. *Proceedings of the National Academy of Sciences* 2015:201523397.

52. Young DJN, et al. (2017) Long-term climate and competition explain forest mortality patterns under extreme drought. *Ecology Letters* 20(1):78–86.

53. Wood EM, Pidgeon AM, Radeloff VC, Keuler NS (2012) Image texture as a remotely sensed measure of vegetation structure. *Remote Sensing of Environment* 121:516–526.

54. Huang Q, Swatantran A, Dubayah R, Goetz SJ (2014) The influence of vegetation height heterogeneity on forest and woodland bird species richness across the United States. *PLoS ONE* 9(8). doi:10.1371/journal.pone.0103236.

55. Stein A, Gerstner K, Kreft H (2014) Environmental heterogeneity as a universal driver of species richness across taxa, biomes and spatial scales. *Ecology Letters* 17(7):866–880.

56. Tuanmu M-N, Jetz W (2015) A global, remote sensing-based characterization of terrestrial habitat heterogeneity for biodiversity and ecosystem modelling. *Global Ecology and Biogeography* 24(11):1329–1339.

57. Kéfi S, et al. (2014) Early warning signals of ecological transitions: Methods for spatial patterns. *PLoS ONE* 9(3):10–13.

58. Haralick RM, Shanmugam K, Dinstein I (1973) Textural Features for Image Classification. *IEEE Transactions on Systems, Man, and Cybernetics* SMC-3(6):610–621.

59. Calkin DE, Gebert KM, Jones J., Neilson RP (2005) Forest service large fire area burned and suppression expenditure trends, 1970-2002. *Journal of Forestry* 103(4):179–183.

60. Vehtari A, Gelman A, Gabry J (2016) Practical Bayesian model evaluation using leave-one-out cross-validation and WAIC. *Statistics and Computing* (June):1–20.

61. Gelman A, Goodrich B, Gabry J, Ali I (2018) R-squared for Bayesian regression models. *unpublished; available http://wwwstatcolumbiaedu/~gelman/research/unpublished/bayes_R2_v3pdf*. Available at: http://www.stat.columbia.edu/{~}gelman/research/unpublished/bayes{_}R2.pdf.

62. Heffernan JB, et al. (2014) Macrosystems ecology: Understanding ecological patterns and processes at continental scales. *Frontiers in Ecology and the Environment* 12(1):5–14.

63. Beck J, et al. (2012) What's on the horizon for macroecology? *Ecography* 35(8):673–683.

64. Lydersen JM, Collins BM, Knapp EE, Roller GB, Stephens S (2015) Relating fuel loads to overstorey structure and composition in a fire-excluded Sierra Nevada mixed conifer forest. *International Journal of Wildland Fire* 24(4):484–494.

65. Collins BM, et al. (2016) Variability in vegetation and surface fuels across mixed-conifer-dominated landscapes with over 40 years of natural fire. *Forest Ecology and Management* 381:74–83.

66. Stephens SL, et al. (2012) The Effects of Forest Fuel-Reduction Treatments in the United States. *BioScience* 62(6):549–560.

67. Parks SA, et al. (2018) High-severity fire: Evaluating its key drivers and mapping its probability across western US forests. *Environmental Research Letters* 13(4). doi:10.1088/1748-9326/aab791.

68. Holden ZA, Morgan P, Evans JS (2009) A predictive model of burn severity based on 20-year satellite-inferred burn severity data in a large southwestern US wilderness area. *Forest Ecology and Management* 258(11):2399–2406.

69. Dillon GK, et al. (2011) Both topography and climate affected forest and woodland burn severity in two regions of the western US, 1984 to 2006. *Ecosphere* 2(12):130.

70. Van Wagner CE (1977) Conditions for the start and spread of crown fire. *Canadian Journal of Forest Research* 7:23–34.

71. Agee JK (1996) The influence of forest structure on fire behavior. *Proceedings of the 17th Annual Forest Vegetation Management Conference*:52–68.

72. Larson AJ, Churchill D (2012) Tree spatial patterns in fire-frequent forests of western North America, including mechanisms of pattern formation and implications for designing fuel reduction and restoration treatments. *Forest Ecology and Management* 267:74–92.

73. Malone SL, et al. (2018) Mixed-severity fire fosters heterogeneous spatial patterns of conifer regeneration in a dry conifer forest. *Forests* 9(1). doi:10.3390/f9010045.

74. Walker RB, Coop JD, Parks SA, Trader L (2018) Fire regimes approaching historic norms reduce wildfire-facilitated conversion from forest to non-forest. *Ecosphere* 9(4). doi:10.1002/ecs2.2182.

75. Van Wagtendonk JW (2006) Fire as a physical process. *Fire in California's Ecosystems*, eds Sugihara

NG, Van Wagtendonk JW, Shaffer KE, Fites-Kaufman J, Thode AE (University of California Press, Berkeley; Los Angeles, CA, USA), pp 38–57. 1st Ed.

76. Coppoletta M, Merriam KE, Collins BM (2016) Post-fire vegetation and fuel development influences fire severity patterns in reburns. *Ecological Applications* 26(3):686–699.

77. Stephens SL, et al. (2013) Managing forests and fire in changing climates. *Science* 342(6154):41–2.

78. Miller JD, Safford HD (2017) Corroborating evidence of a pre-euro-American low-to moderate-severity fire regime in yellow pine–mixed conifer forests of the sierra Nevada, California, USA. *Fire Ecology* 13(1):58–90.

79. Safford HD, Stevens JT, Merriam K, Meyer MD, Latimer AM (2012) Fuel treatment effectiveness in California yellow pine and mixed conifer forests. *Forest Ecology and Management* 274:17–28.

80. Stephens SL, et al. (2013) Fire Treatment Effects on Vegetation Structure, Fuels, and Potential Fire Severity in Western U. S. Forests. *Ecological Applications* 19(2):305–320.

81. Peters DPC, et al. (2004) Cross-scale interactions, nonlinearities, and forecasting catastrophic events. 101(42).

82. Lydersen JM, North MP, Collins BM (2014) Severity of an uncharacteristically large wildfire, the Rim Fire, in forests with relatively restored frequent fire regimes. *Forest Ecology and Management* 328:326–334.

83. Gorelick N, et al. (2017) Remote Sensing of Environment Google Earth Engine : Planetary-scale geospatial analysis for everyone. *Remote Sensing of Environment* 202:18–27.

84. Key CH, Benson NC (2006) Landscape assessment: Sampling and analysis methods. *USDA Forest Service General Technical Report RMRS-GTR-164-CD* (June):1–55.

85. Zhu Z, Key C, Ohlen D, Benson N (2006) Evaluate Sensitivities of Burn-Severity Mapping Algorithms for Different Ecosystems and Fire Histories in the United States. *Final Report to the Joint Fire Science Program, Project JFSP 01-1-4-12*:1–35.

86. (eds.) JFP (2016) Jepson eFlora. Available at: http://ucjeps.berkeley.edu/eflora/ [Accessed March 7, 2016].

87. Masek JG, et al. (2006) A Landsat Surface Reflectance Dataset. *IEEE Geoscience and Remote Sensing Letters* 3(1):68–72.

88. Vermote E, Justice C, Claverie M, Franch B (2016) Preliminary analysis of the performance of the Landsat 8/OLI land surface reflectance product. *Remote Sensing of Environment* 185:46–56.

89. USGS (2017) Product Guide: Landsat 4-7 Surface Reflectance (LEDAPS) Product. *USGS Professional Paper* 8(1):38.

90. USGS (2017) Product Guide: Landat 8 Surface Reflectance Code (LaSRC) Product. *USGS Professional Paper* 4.2.

91. Miller JD, Skinner CN, Safford HD, Knapp EE, Ramirez CM (2012) Trends and causes of severity, size, and number of fires in northwestern California, USA. *Ecological Applications* 22(1):184–203.

92. Miller JD, Safford H (2012) Trends in wildfire severity: 1984 to 2010 in the Sierra Nevada, Modoc Plateau, and southern Cascades, California, USA. *Fire Ecology* 8(3):41–57.

93. Foga S, et al. (2017) Remote Sensing of Environment Cloud detection algorithm comparison and validation for operational Landsat data products. *Remote Sensing of Environment* 194:379–390.

94. García MJL, Caselles V (1991) Mapping burns and natural reforestation using thematic mapper data. *Geocarto International* 6(1):31–37.

95. Sikkink PG, et al. (2013) *Composite Burn Index (CBI) data and field photos collected for the FIRESEV project, western United States* (Forest Service Research Data Archive, Fort Collins, CO) doi:10.2737/RDS-2013-0017.

96. Wickham H (2017) *modelr: Modelling Functions that Work with the Pipe* Available at: https://cran.r-project.org/package=modelr.

97. Henry L, Wickham H (2018) *purrr: Functional Programming Tools* Available at: https://cran.r-project.org/package=purrr.

98. R Core Team (2018) *R: A language and environment for statistical computing. http://www.r-project.org/* (R Foundation for Statistical Computing, Vienna, Austria) Available at: http://www.r-project.org/.

99. Franklin J, Logan TL, Woodcock CE, Strahler AH (1986) Forest Classification and Inventory System Using Landsat, Digital Terrain, and Ground Sample Data. *IEEE Transactions on Geoscience and Remote Sensing* GE-24(1):139–149.

100. Farr T, et al. (2007) The shuttle radar topography mission. *Reviews of Geophysics* 45(2005):1–33.

101. McCune B, Keon D (2002) Equations for potential annual direct incident radiation and heat load. *Journal of Vegetation Science* 13(1966):603–606.

102. McCune B (2007) Improved estimates of incident radiation and heat load using non-parametric regression against topographic variables. *Journal of Vegetation Science* 18(2002):751–754.

103. Abatzoglou JT (2013) Development of gridded surface meteorological data for ecological applications and modelling. *International Journal of Climatology* 33(1):121–131.

104. Hoffman MD, Gelman A (2014) The No-U-Turn Sampler: Adaptively Setting Path Lengths in Hamiltonian Monte Carlo. *Journal of Machine Learning Research* 15:1593–1623.

105. Bürkner P-C (2017) brms : An R Package for Bayesian Multilevel Models Using Stan. *Journal of Statistical Software* 80(1). doi:10.18637/jss.v080.i01.

Supplemental information

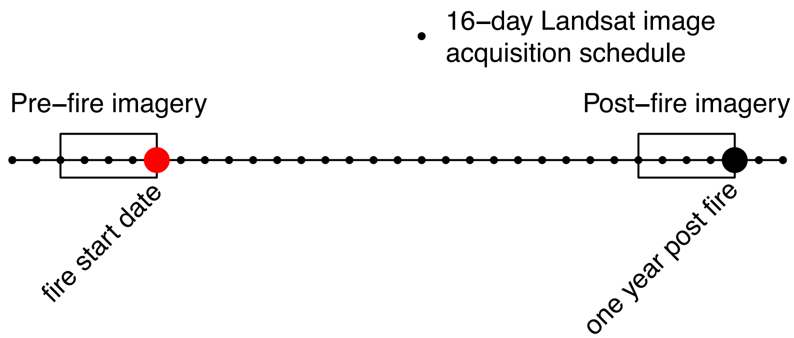

Supplementary Figure 1. Schematic for how Landsat imagery was assembled in order to make comparisons between pre- and post-fire conditions. This schematic depicts a 64-day window of image collation prior to the fire which comprise the pre-fire image collection. A similar, 64-day window collection of imagery is assembled one year after the pre-fire image collection.

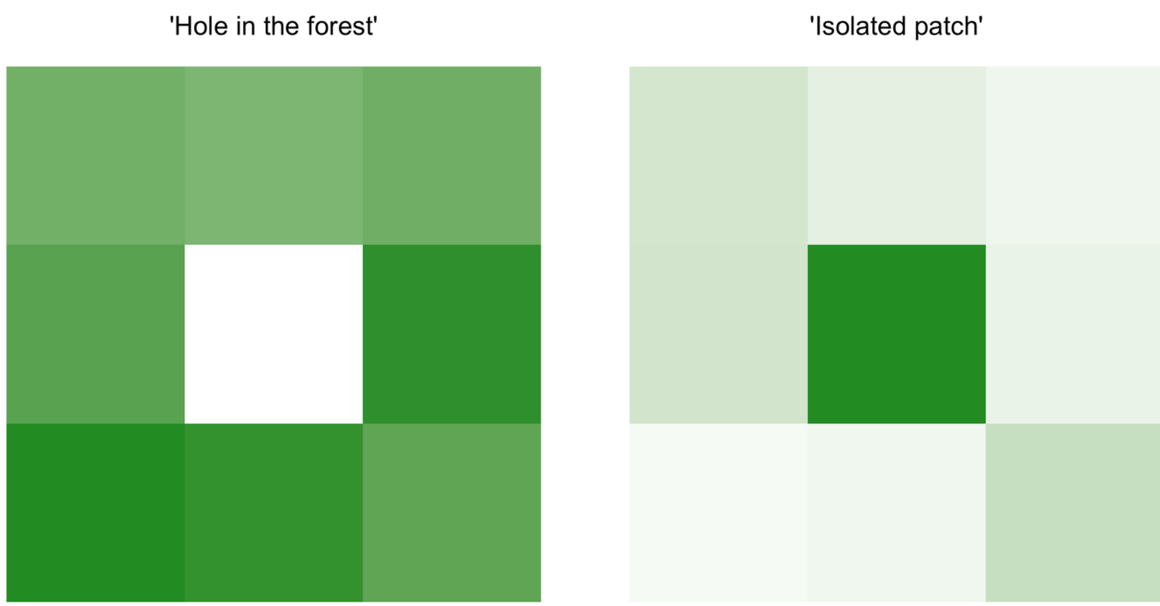

Supplementary Figure 2. Conceptual diagram of 'decoupling' that sometimes occurs between the central pixel NDVI and the neighborhood mean NDVI. In each of these scenarios, our model results suggest that the probability that the central pixel burns at high severity is higher than expected given the additive effect of the covariates. The left panel depicts the "hole in the forest" decoupling, which occurs more frequently, and the right panel depicts the "isolated patch" decoupling.

Supplemental methods

Normalized difference vegetation index (NDVI; Supplementary Eq. 1) correlates with vegetation density, canopy cover, and leaf area index (1). Normalized difference moisture index (NDMI; Supplementary Eq. 2) correlates with similar vegetation characteristics as NDVI, but doesn't saturate at high levels of foliar biomass (2). Normalized burn ratio (NBR; Supplementary Eq. 3) and normalized burn ratio version 2 (NBR2; Supplementary Eq. 4) respond strongly to fire effects on vegetation (4–8).

(1) $ndvi = (nir - red)/(nir + red)$

(2) $ndmi = (nir - swir1)/(nir + swir1)$

(3) $nbr = (nir - swir2)/(nir + swir2)$

(4) $nbr2 = (swir1 - swir2)/(swir1 + swir2)$

Where nir is the near infrared band (band 4 on Landsat 4, 5, and 7; band 5 on Landsat 8) and red is the red band (band 3 on Landsat 4, 5, and 7; band 4 on Landsat 8), $swir1$ is the first short wave infrared band (band 5 on Landsat 4, 5, and 7; band 4 on Landsat 8), $swir2$ is the second short wave infrared band (band 7 on Landsat 4, 5, 7, and 8)

We calculated the delta severity indices (dNBR, dNBR2, dNDVI) by subtracting the respective postfire indices from the prefire indices (NBR, NBR2, and NDVI) without multiplying by a rescaling constant (e.g., we did not multiply the result by 1000 as in (9); Supplementary Eq. 5). Following (10), we chose not to correct the delta indices using a phenological offset value (typically calculated as the delta index in homogeneous forest patch outside of the fire perimeter), as our approach implicitly accounts for phenology by incorporating multiple cloud-free images across the same time window both before the fire and one year later.

$$\text{(5)} \quad dI = I_{\text{prefire}} - I_{\text{postfire}}$$

We calculated the relative delta severity indices, RdNBR and RdNDVI, by scaling the respective delta indices (dNBR and dNDVI) from Supplementary Eq. 6 by a square root transformation of the absolute value of the prefire index:

$$\text{(6)} \quad RdI = \frac{dI}{\sqrt{|I_{\text{prefire}}|}}$$

We calculated the relative burn ratio (RBR) following (11) using Supplementary Eq. 7:

$$\text{(7)} \quad RBR = \frac{dNBR}{NBR_{\text{prefire}} + 1.001}$$

We used the digital elevation model to calculate the potential annual heat load (Supplementary Eq. 8 at each pixel, which is an integrated measure of latitude, slope, and a folding transformation of aspect about the northeast-southwest line, such that northeast becomes 0 radians and southwest becomes π radians (12, 13):

$$\text{(8)} \quad \begin{aligned} aspect_{folded} &= \left|\pi - \left|aspect - \frac{5\pi}{4}\right|\right| \\ log(pahl) &= \begin{array}{l} -1.467 + \\ 1.582 * cos(latitude)cos(slope) - \\ 1.5 * cos(aspect_{folded})sin(slope)sin(latitude) - \\ 0.262 * sin(lat)sin(slope) + \\ 0.607 * sin(aspect_{folded})sin(slope) \end{array} \end{aligned}$$

Where $pahl$ is the potential annual heat load, $aspect_{folded}$ is a transformation of aspect in radians, and both $latitude$ and $slope$ are extracted from a digital elevation model with units of radians.

Supplementary Table 1. *Comparison of models used to validate and calibrate remotely sensed wildfire severity with ground based composite burn index (CBI) severity sorted in descending order by the R^2 value from a 5-fold cross validation. A total of 56 models were tested representing all possible combinations of 7 different measures of wildfire severity (RBR, dNBR, dNBR2, RdNBR, RdNBR2, dNDVI, and RdNDVI), 4 different time windows in which Landsat imagery was acquired and summarized with a median reducer on a pixel-by-pixel basis (16 days, 32 days, 48 days, and 64 days), and two different interpolation methods (bilinear and bicubic). The three parameters (β_0, β_1 , and β_2) from the nonlinear model fit described in Eq. 1 are reported. For each model, the value of the remotely sensed wildfire severity measurement corresponding to the lower bounds of 3 commonly used categories of severity are reported ('low' corresponds to a CBI value of 0.1, 'mod' corresponds to a CBI value of 1.25, and 'high' corresponds to a CBI value of 2.25)*

Rank			Interpolation		β_0	β_1	β_2	low	mod	high
1	RBR	48	bicubic	0.820	0.014	0.028	1.001	0.045	0.113	0.282
2	RdNBR	32	bilinear	0.813	-0.483	3.061	0.857	2.852	8.450	20.559
3	RdNDVI	48	bilinear	0.809	-2.144	3.273	0.609	1.335	4.867	10.753
4	RBR	32	bilinear	0.807	0.014	0.029	0.985	0.046	0.113	0.280
5	RdNDVI	64	bicubic	0.805	-2.524	3.570	0.590	1.263	4.936	10.929
6	RBR	64	bicubic	0.805	0.016	0.027	1.010	0.046	0.113	0.283
7	RdNDVI	32	bicubic	0.803	-2.737	3.308	0.619	0.782	4.436	10.586
8	RBR	64	bilinear	0.802	0.017	0.027	1.003	0.047	0.113	0.279
9	RdNDVI	32	bilinear	0.801	-2.531	3.176	0.624	0.849	4.393	10.387
10	RdNDVI	48	bicubic	0.797	-2.623	3.624	0.587	1.220	4.922	10.943
11	RdNDVI	64	bilinear	0.796	-2.140	3.287	0.607	1.353	4.876	10.728
12	RdNBR	64	bilinear	0.792	-0.420	3.031	0.862	2.884	8.483	20.663
13	RBR	48	bilinear	0.791	0.017	0.027	1.006	0.047	0.112	0.277

14	RBR	32	bicubic	0.790	0.013	0.029	0.994	0.045	0.114	0.284
15	RdNBR	48	bicubic	0.785	-0.858	3.219	0.852	2.647	8.476	21.021
16	RBR	16	bilinear	0.781	0.021	0.026	1.016	0.050	0.114	0.278
17	RdNBR	32	bicubic	0.776	-0.954	3.340	0.841	2.679	8.602	21.199
18	dNDVI	32	bicubic	0.776	-0.058	0.073	0.650	0.020	0.106	0.257
19	dNBR	48	bicubic	0.775	0.030	0.035	1.069	0.068	0.161	0.413
20	RdNBR	16	bilinear	0.774	0.279	2.518	0.909	3.037	8.119	19.727
21	dNDVI	32	bilinear	0.772	-0.053	0.070	0.656	0.022	0.105	0.252
22	dNDVI	48	bicubic	0.772	-0.055	0.081	0.613	0.031	0.119	0.267
23	dNBR	32	bilinear	0.770	0.029	0.036	1.048	0.069	0.163	0.410
24	RdNBR2	64	bicubic	0.766	2.102	0.416	1.240	2.572	4.059	8.861
25	dNBR	32	bicubic	0.764	0.028	0.036	1.057	0.068	0.163	0.417
26	dNDVI	48	bilinear	0.762	-0.044	0.073	0.637	0.034	0.118	0.262
27	RBR	16	bicubic	0.761	0.021	0.026	1.028	0.049	0.114	0.281
28	dNBR	16	bilinear	0.760	0.033	0.036	1.048	0.073	0.167	0.417
29	RdNBR2	32	bilinear	0.759	1.435	0.625	1.100	2.132	3.906	8.861
30	RdNBR	16	bicubic	0.758	0.370	2.446	0.926	3.053	8.149	19.999
31	RdNBR2	32	bicubic	0.754	1.426	0.601	1.125	2.098	3.876	8.975
32	dNBR	64	bicubic	0.753	0.033	0.033	1.086	0.070	0.161	0.413

33	dNBR	64	bilinear	0.751	0.035	0.033	1.080	0.071	0.161	0.406
34	RdNBR2	48	bicubic	0.751	1.835	0.460	1.209	2.354	3.919	8.818
35	dNBR	48	bilinear	0.748	0.035	0.033	1.076	0.071	0.161	0.405
36	RdNDVI	16	bilinear	0.747	-0.983	2.503	0.678	1.695	4.856	10.515
37	dNDVI	64	bicubic	0.746	-0.055	0.082	0.609	0.032	0.120	0.266
38	dNDVI	64	bilinear	0.741	-0.046	0.075	0.627	0.034	0.118	0.261
39	RdNBR2	48	bilinear	0.737	1.802	0.497	1.174	2.361	3.956	8.766
40	RdNBR	64	bicubic	0.737	-1.448	3.651	0.819	2.515	8.717	21.611
41	RdNBR2	64	bilinear	0.735	2.027	0.451	1.204	2.536	4.060	8.801
42	dNBR	16	bicubic	0.729	0.032	0.036	1.058	0.072	0.168	0.423
43	dNBR2	32	bilinear	0.727	0.026	0.009	1.149	0.035	0.062	0.140
44	dNDVI	16	bicubic	0.726	-0.030	0.065	0.674	0.040	0.121	0.267
45	RdNDVI	16	bicubic	0.725	-1.248	2.681	0.665	1.618	4.908	10.721
46	dNBR2	32	bicubic	0.715	0.025	0.008	1.177	0.035	0.061	0.142
47	dNBR2	64	bilinear	0.714	0.036	0.006	1.283	0.043	0.064	0.137
48	dNDVI	16	bilinear	0.707	-0.023	0.060	0.689	0.042	0.120	0.261
49	dNBR2	48	bilinear	0.686	0.033	0.006	1.248	0.040	0.063	0.137
50	RdNBR2	16	bilinear	0.682	1.928	0.465	1.189	2.452	3.983	8.676
51	dNBR2	16	bilinear	0.662	0.030	0.009	1.138	0.040	0.066	0.143

52	RdNBR2	16	bicubic	0.654	1.871	0.467	1.198	2.398	3.960	8.792
53	dNBR2	16	bicubic	0.635	0.029	0.009	1.156	0.039	0.066	0.145
54	RdNBR	48	bilinear	0.630	-3.445	5.132	0.724	2.072	9.235	22.700
55	dNBR2	48	bicubic	0.000	0.033	0.006	1.284	0.040	0.062	0.138
56	dNBR2	64	bicubic	0.000	0.037	0.005	1.313	0.043	0.064	0.139

Supplementary Table 2. Estimates of cofficients for logistic mixed effects model described in Eq. 10. Coefficient estimates are given, along with their 95% credible intervals, for each of four different models fit using data from different neighborhood sizes. The values of three variables (standard deviation of NDVI within a neighborhood, mean of NDVI within a neighborhood, and topographic roughness) depended on neighborhood size and thus the four different models are fit to the same data except for those three variables.

Coefficient	90m x 90m neighborhood estimate (95% CI)	150m x 150m neighborhood estimate (95% CI)	210m x 210m neighborhood estimate (95% CI)	270m x 270m neighborhood estimate (95% CI)
β_0	-2.415 (-2.588, -2.255)	-2.432 (-2.605, -2.271)	-2.447 (-2.619, -2.279)	-2.45 (-2.618, -2.288)
$\beta_{nbhd\_stdev\_NDVI}$	-0.208 (-0.247, -0.17)	-0.212 (-0.255, -0.17)	-0.203 (-0.248, -0.158)	-0.195 (-0.242, -0.148)
$\beta_{prefire\_NDVI}$	1.044 (0.911, 1.174)	1.13 (1.028, 1.229)	1.141 (1.057, 1.222)	1.132 (1.056, 1.209)
β_{fm100}	-0.569 (-0.71, -0.423)	-0.564 (-0.709, -0.419)	-0.561 (-0.697, -0.428)	-0.565 (-0.712, -0.422)
β_{pahl}	0.239 (0.208, 0.271)	0.238 (0.205, 0.269)	0.239 (0.207, 0.269)	0.24 (0.209, 0.272)
$\beta_{topographic\_roughness}$	-0.01 (-0.042, 0.022)	-0.006 (-0.039, 0.027)	-0.002 (-0.037, 0.032)	-0.002 (-0.036, 0.033)
$\beta_{nbhd\_mean\_NDVI}$	-0.14 (-0.278, 0.002)	-0.265 (-0.381, -0.148)	-0.293 (-0.392, -0.193)	-0.293 (-0.389, -0.198)
$\beta_{nbhd\_stdev\_NDVI*prefire\_NDVI}$	0.125 (0.029, 0.218)	0.06 (-0.013, 0.135)	0.022 (-0.045, 0.09)	0.009 (-0.054, 0.072)
$\beta_{nbhd\_stdev\_NDVI*nbhd\_mean\_NDVI}$	-0.129 (-0.223, -0.034)	-0.078 (-0.151, -0.006)	-0.03 (-0.095, 0.035)	-0.006 (-0.068, 0.054)
$\beta_{nbhd\_stdev\_NDVI*fm100}$	-0.037 (-0.081, 0.006)	-0.035 (-0.078, 0.01)	-0.03 (-0.076, 0.014)	-0.023 (-0.07, 0.023)
$\beta_{nbhd\_mean\_NDVI*prefire\_NDVI}$	-0.573 (-0.62, -0.526)	-0.564 (-0.612, -0.516)	-0.549 (-0.596, -0.502)	-0.537 (-0.587, -0.49)

Supplemental References

1. Rouse JW, Hass RH, Schell J, Deering D (1973) Monitoring vegetation systems in the great plains with ERTS. *Third Earth Resources Technology Satellite (ERTS) symposium* 1:309–317.

2. Gao BC (1996) NDWI - A normalized difference water index for remote sensing of vegetation liquid water from space. *Remote Sensing of Environment* 58(3):257–266.

3. Huesca M, García M, Roth KL, Casas A, Ustin SL (2016) Canopy structural attributes derived from AVIRIS imaging spectroscopy data in a mixed broadleaf/conifer forest. *Remote Sensing of Environment* 182:208–226.

4. García MJL, Caselles V (1991) Mapping burns and natural reforestation using thematic mapper data. *Geocarto International* 6(1):31–37.

5. Key CH, Benson NC (2006) Landscape assessment: Sampling and analysis methods. *USDA Forest Service General Technical Report RMRS-GTR-164-CD* (June):1–55.

6. USGS (2017) Product Guide: Landat 8 Surface Reflectance Code (LaSRC) Product. *USGS Professional Paper* 4.2.

7. USGS (2017) Product Guide: Landsat 4-7 Surface Reflectance (LEDAPS) Product. *USGS Professional Paper* 8(1):38.

8. Hawbaker TJ, et al. (2017) Mapping burned areas using dense time-series of Landsat data. *Remote Sensing of Environment* 198:504–522.

9. Miller JD, Thode AE (2007) Quantifying burn severity in a heterogeneous landscape with a relative version of the delta Normalized Burn Ratio (dNBR). *Remote Sensing of Environment* 109:66–80.

10. Reilly MJ, et al. (2017) Contemporary patterns of fire extent and severity in forests of the Pacific Northwest, USA (1985-2010). *Ecosphere* 8(3). doi:10.1002/ecs2.1695.

11. Parks SA, Dillon GK, Miller C (2014) A new metric for quantifying burn severity: The relativized burn ratio. *Remote Sensing* 6(3):1827–1844.

12. McCune B, Keon D (2002) Equations for potential annual direct incident radiation and heat load. *Journal of Vegetation Science* 13(1966):603–606.

13. McCune B (2007) Improved estimates of incident radiation and heat load using non-parametric regression against topographic variables. *Journal of Vegetation Science* 18(2002):751–754.